

Deformed Coordinate-Space Hartree-Fock-Bogoliubov Approach to Weakly Bound Nuclei and Large Deformations

J.C. Pei,^{1,2,3} M.V. Stoitsov,^{2,3,4} G.I. Fann,³ W. Nazarewicz,^{2,3,5} N. Schunck,^{2,3} and F.R. Xu⁶

¹*Joint Institute for Heavy Ion Research, Oak Ridge, TN 37831, USA*

²*Department of Physics and Astronomy, University of Tennessee, Knoxville, TN 37996, USA*

³*Oak Ridge National Laboratory, P.O. Box 2008, Oak Ridge, TN 37831, USA*

⁴*Institute of Nuclear Research and Nuclear Energy, Bulgarian Academy of Sciences, Sofia, Bulgaria*

⁵*Institute of Theoretical Physics, Warsaw University, ul.Hoża 69, PL-00681 Warsaw, Poland*

⁶*State Key Laboratory of Nuclear Physics and Technology, School of Physics, Peking University, Beijing 100871, China*

(Dated: July 18, 2008)

The coordinate space formulation of the Hartree-Fock-Bogoliubov (HFB) method enables self-consistent treatment of mean-field and pairing in weakly bound systems whose properties are affected by the particle continuum space. Of particular interest are neutron-rich, deformed drip-line nuclei which can exhibit novel properties associated with neutron skin. To describe such systems theoretically, we developed an accurate 2D lattice Skyrme-HFB solver HFB-AX based on B-splines. Compared to previous implementations, we made a number of improvements aimed at boosting the solver's performance. These include: explicit imposition of axiality and space inversion, use of the modified Broyden's method to solve self-consistent equations, and a partial parallelization of the code. HFB-AX has been benchmarked against other HFB solvers, both spherical and deformed, and the accuracy of the B-spline expansion was tested by employing the multiresolution wavelet method. Illustrative calculations are carried out for stable and weakly bound nuclei at spherical and very deformed shapes, including constrained fission pathways. In addition to providing new physics insights, HFB-AX can serve as a useful tool to assess the reliability and applicability of coordinate-space and configuration-space HFB solvers, both existing and in development.

PACS numbers: 21.60.Jz, 21.10.-k, 02.70.-c, 31.15.ej

I. INTRODUCTION

The important new focus in theoretical nuclear structure research is to develop a coherent theoretical framework aiming at the microscopic description of nuclear many-body systems and capable of extrapolating into unknown regions. An important component in the theoretical landscape, and a crucial part of the theory roadmap [1, 2], is the nuclear Density Functional Theory (DFT) in the formulation of Kohn and Sham [3]. Since the majority of nuclei in their ground states are superconductors, pairing correlations have to be taken into account. The resulting HFB or Bogoliubov de-Gennes equations can be viewed as the generalized Kohn-Sham equations of the standard DFT. The main ingredient of the nuclear DFT [4, 5] is the energy density functional that depends on proton and neutron densities and currents, as well as pairing densities representing correlated nucleonic pairs [6].

The unique structural factor that determines many properties of weakly bound nuclei is the closeness of the particle continuum. While the nuclear densities of bound nuclei eventually vanish at large distances, the wave functions of positive-energy states do not decay outside the nuclear volume, and this can be a source of significant theoretical difficulties. This problem is naturally overcome in the HFB method with a realistic pairing interaction in which the coupling of bound states to the particle continuum is correctly taken into account. In this con-

text, particularly useful is the coordinate-space formulation of HFB [7, 8]. Another advantage of this method is its ability to treat arbitrarily complex intrinsic shapes, including those seen in fission or fusion.

The HFB equations of the nuclear DFT represent the self-consistent iterative convergence schemes. Their computational cost can become very expensive, especially when the size of the model space – largely determined by the self-consistent symmetries imposed – or the number of nuclear configurations processed simultaneously is huge. The advent of teraflop computers makes such large-scale calculations feasible, but in order to better optimize unique resources, new-generation tools are called for.

A number of coordinate-space approaches to the nuclear DFT have been developed over the years, and their performance strongly depends on the size and symmetries of the spatial mesh employed [9, 10, 11]. The EV8 code solves the Hartree-Fock plus BCS equations for Skyrme-type functionals via a discretization of the individual wave-functions on a 3D Cartesian mesh [12], assuming three symmetry planes. The 1D HFBRAD finite-difference code has been developed as a standard tool for HFB calculations of spherical nuclei [13]. While limited to the radial coordinate only, HFBRAD allows very precise calculations, as the mesh step can be taken very low. The recently developed parallel 2D HFB-2D-LATTICE code [14, 15, 16] is based on B-splines; it can treat axially deformed nuclei, *including* those with reflection-asymmetric shapes. No coordinate-space 3D HFB nu-

clear framework exists at present; however, a number of developments are under way, including a general-purpose HFB solver based on wavelet technology [17, 18].

One traditional way of solving the HFB problem is to use the configuration-space technique, in which HFB eigenstates are expanded in a discrete basis, such as the harmonic oscillator (HO) basis [19]. This method is very efficient and has been applied successfully in the large-scale calculations of nuclear properties [20]. However, the use of the HO basis is questionable in the limit of weak binding (because of incorrect asymptotic behavior of HO states) and at very large deformations, both requiring the use of unrealistically large configuration spaces. In both situations, a coordinate-state description is superior.

The main objective of this paper is to develop a reliable and accurate HFB axial solver, based on B-splines, to study weakly bound nuclei and/or constrained energy surfaces involving very large deformations. An HFB scheme based on such a concept has been implemented in HFB-2D-LATTICE by the Vanderbilt group [14, 15, 16]. An attractive feature of HFB-2D-LATTICE is that by taking high-order B-splines one guarantees the correct representation of derivative operators on the spatial lattice [9]. Unfortunately, the performance of HFB-2D-LATTICE is strongly CPU-limited. To speed up the calculations, and at the same time to improve the accuracy, we wrote a new 2D HFB B-spline code, called HFB-AX, in which a number of new features were introduced. Firstly, we incorporated space inversion as a self-consistent symmetry. Since reflection-asymmetric ground-state deformations are present only in a handful of nuclei, this is not a serious limitation. Furthermore, we improved the iterative algorithm by means of the modified Broyden's method. This resulted in significant convergence acceleration. We also made a number of smaller optimizations to the HFB solver which are described in the text. The performance and accuracy of HFB-AX has been very carefully tested against other codes. In short, we developed a fast, deformed coordinate-space HFB solver that can be used to carry out large-scale calculations on leadership-class computers, and it can also be invaluable when benchmarking the next-generation nuclear DFT tools.

This paper is organized as follows. Section II shortly summarizes the coordinate-space HFB approach in the cylindrical coordinate system and describes the numerical method used. In Sec. III, numerical tests are presented, with an emphasis on benchmarking against other existing HFB solvers. The examples include: (i) a two-center potential problem and a comparison with the multiresolution wavelet method and the HO expansion technique; (ii) comparison with the spherical finite-difference solver HFB-RAD for stable ^{120}Sn and drip-line Ni isotopes; (iii) study of neutron-rich deformed $^{102,110}\text{Zr}$ and comparison with the axial solvers HFB-THO and HFB-2D-LATTICE; and (iv) fission path calculations for ^{240}Pu . Finally, Sec. IV contains the main conclusions of this paper.

II. THEORETICAL FRAMEWORK AND NUMERICAL METHOD

A. HFB equation in cylindrical coordinate space

The HFB equations in the coordinate-space representation can be written as [7, 8, 21]:

$$\int d\mathbf{r}' \sum_{\sigma'} \begin{pmatrix} h(\mathbf{r}\sigma, \mathbf{r}'\sigma') - \lambda & \tilde{h}(\mathbf{r}\sigma, \mathbf{r}'\sigma') \\ \tilde{h}(\mathbf{r}\sigma, \mathbf{r}'\sigma') & -h(\mathbf{r}\sigma, \mathbf{r}'\sigma') + \lambda \end{pmatrix} \times \begin{pmatrix} \psi^{(1)}(\mathbf{r}'\sigma') \\ \psi^{(2)}(\mathbf{r}'\sigma') \end{pmatrix} = E \begin{pmatrix} \psi^{(1)}(\mathbf{r}\sigma) \\ \psi^{(2)}(\mathbf{r}\sigma) \end{pmatrix}, \quad (1)$$

where (\mathbf{r}, σ) are the particle spatial and spin coordinates, $h(\mathbf{r}\sigma, \mathbf{r}'\sigma')$ and $\tilde{h}(\mathbf{r}\sigma, \mathbf{r}'\sigma')$ are the particle-hole (p-h) and particle-particle (p-p) components of the single-quasiparticle Hamiltonian, respectively, $\psi_n^{(1)}(\mathbf{r}\sigma)$ and $\psi_n^{(2)}(\mathbf{r}\sigma)$ are the upper and lower components of the single-quasiparticle HFB wave function, and λ is the chemical potential. The spectrum of quasiparticle energies E is discrete for $|E| < -\lambda$ and continuous for $|E| > -\lambda$. With the box boundary conditions, the continuum is discretized. In practical calculations, the p-h channel is often modeled with the Skyrme energy density functional, while a zero-range δ pairing interaction is used in the p-p channel. This choice is motivated by the fact that zero-range interactions yield the local HFB equations in coordinate space which are easy to solve.

In the axially symmetric geometry, the third component of the single-particle angular momentum, Ω , is a good quantum number. The HFB wave function can thus be written as $\Psi_n(\mathbf{r}, \Omega, q)$ where $\mathbf{r}=(\phi, \rho, z)$, $q=\pm\frac{1}{2}$ denotes the cylindrical isospin coordinates, and $\Omega=\pm\frac{1}{2}, \pm\frac{3}{2}, \pm\frac{5}{2}, \dots$. The corresponding HFB wave function can be written as [14],

$$\begin{aligned} \Psi_n(\mathbf{r}, \Omega, q) &= \begin{pmatrix} \psi_{n,\Omega,q}^{(1)}(\phi, \rho, z) \\ \psi_{n,\Omega,q}^{(2)}(\phi, \rho, z) \end{pmatrix} \\ &= \frac{1}{\sqrt{2\pi}} \begin{pmatrix} e^{i(\Omega-\frac{1}{2})\phi} \psi_{n,\Omega,q}^{(1)}(\rho, z, \uparrow) \\ e^{i(\Omega+\frac{1}{2})\phi} \psi_{n,\Omega,q}^{(1)}(\rho, z, \downarrow) \\ e^{i(\Omega-\frac{1}{2})\phi} \psi_{n,\Omega,q}^{(2)}(\rho, z, \uparrow) \\ e^{i(\Omega+\frac{1}{2})\phi} \psi_{n,\Omega,q}^{(2)}(\rho, z, \downarrow) \end{pmatrix}. \end{aligned} \quad (2)$$

Following the notation of Ref. [14], we introduce

$$\begin{aligned} U_{n\Omega q}^{(1,2)}(\rho, z) &= \psi_{n\Omega q}^{(1,2)}(\rho, z, \uparrow), \\ D_{n\Omega q}^{(1,2)}(\rho, z) &= \psi_{n\Omega q}^{(1,2)}(\rho, z, \downarrow), \end{aligned} \quad (3)$$

where wave functions U and D denote the spin-up ($\sigma=\frac{1}{2}$) and spin-down ($\sigma=-\frac{1}{2}$) spinor components. Since the time reversal symmetry is conserved, one can consider only positive- Ω values. In terms of these wave functions,

the particle density $\rho_q(\mathbf{r})$ and pairing density $\tilde{\rho}_q(\mathbf{r})$ can be written as:

$$\begin{aligned}\rho_q(\mathbf{r}) &= \sum_{\sigma} \sum_{n\Omega} \psi_{n\Omega q}^{(2)}(\mathbf{r}\sigma) \psi_{n\Omega q}^{(2)*}(\mathbf{r}\sigma) \\ &= \frac{1}{\pi} \sum_{\Omega=\frac{1}{2}}^{\Omega_{\max}} \sum_{E_n>0}^{E_{\max}} [|U_{n\Omega q}^{(2)}(\rho, z)|^2 \\ &\quad + |D_{n\Omega q}^{(2)}(\rho, z)|^2], \\ \tilde{\rho}_q(\mathbf{r}) &= - \sum_{\sigma} \sum_{n\Omega} \psi_{n\Omega q}^{(2)}(\mathbf{r}\sigma) \psi_{n\Omega q}^{(1)*}(\mathbf{r}\sigma) \\ &= -\frac{1}{\pi} \sum_{\Omega=\frac{1}{2}}^{\Omega_{\max}} \sum_{E_n>0}^{E_{\max}} [U_{n\Omega q}^{(2)}(\rho, z) U_{n\Omega q}^{(1)*}(\rho, z) \\ &\quad + D_{n\Omega q}^{(2)}(\rho, z) D_{n\Omega q}^{(1)*}(\rho, z)].\end{aligned}\quad (4)$$

In the above equations, the sums are limited by the quasi-particle energy cutoff E_{\max} , defining the effective range for a zero-range pairing force, and the angular projection cutoff Ω_{\max} . This way of truncating the continuum space is different from that in the spherical HFBRAD code [13] which employs a maximum j_{\max} cutoff on the total single-particle angular momentum. This implies that even with the same energy cutoff, HFB-AX and HFBRAD have different pairing phase spaces. We shall return to this point later in Sec. III.

TABLE I: Boundary conditions of HFB wave functions at $\rho=0$ and $z=0$ in HFB-AX. The single-particle states are labeled by Ω^π quantum numbers.

	$\rho=0$	$z=0$
$\Omega - \frac{1}{2} = \text{even}$ $\pi = +1$	$\frac{\partial U}{\partial \rho} _{\rho=0} = 0$ $D _{\rho=0} = 0$	$\frac{\partial U}{\partial z} _{z=0} = 0$ $D _{z=0} = 0$
$\Omega - \frac{1}{2} = \text{odd}$ $\pi = +1$	$\frac{\partial D}{\partial \rho} _{\rho=0} = 0$ $U _{\rho=0} = 0$	$\frac{\partial D}{\partial z} _{z=0} = 0$ $U _{z=0} = 0$
$\Omega - \frac{1}{2} = \text{even}$ $\pi = -1$	$\frac{\partial U}{\partial \rho} _{\rho=0} = 0$ $D _{\rho=0} = 0$	$\frac{\partial D}{\partial z} _{z=0} = 0$ $U _{z=0} = 0$
$\Omega - \frac{1}{2} = \text{odd}$ $\pi = -1$	$\frac{\partial D}{\partial \rho} _{\rho=0} = 0$ $U _{\rho=0} = 0$	$\frac{\partial U}{\partial z} _{z=0} = 0$ $D _{z=0} = 0$

In the reflection-symmetric version of the code HFB-AX discussed in this paper, we assumed the space inversion as a self-consistent symmetry. Consequently, the quasiparticle wave functions are eigenstates of the parity operator \hat{P} :

$$\hat{P}\Psi_{n,\Omega,q}(\rho, z, \phi) = \pi\Psi_{n,\Omega,q}(\rho, -z, \phi + \pi), \quad (5)$$

i.e., parity $\pi = \pm$ is a good quantum number. The presence of conserved parity implies specific boundary conditions at $\rho=0$ and $z=0$ (see Table I). We also apply the box boundary conditions at the outer box boundaries; namely, the wave functions are put to zero at the edge of

a 2D box z_{\max} and ρ_{\max} . These boundary conditions are important for the construction of derivative operators.

In a given (Ω, q) block, the HFB Hamiltonian in Eq. (1) can be expressed through the mean fields h and \tilde{h} with specified spin projections [14]:

$$\begin{pmatrix} h_{\uparrow\uparrow} - \lambda & h_{\uparrow\downarrow} & \tilde{h}_{\uparrow\uparrow} & \tilde{h}_{\uparrow\downarrow} \\ h_{\downarrow\uparrow} & h_{\downarrow\downarrow} - \lambda & \tilde{h}_{\downarrow\uparrow} & \tilde{h}_{\downarrow\downarrow} \\ \tilde{h}_{\uparrow\uparrow} & \tilde{h}_{\uparrow\downarrow} & -h_{\uparrow\uparrow} + \lambda & h_{\uparrow\downarrow} \\ \tilde{h}_{\downarrow\uparrow} & \tilde{h}_{\downarrow\downarrow} & h_{\downarrow\uparrow} & -h_{\downarrow\downarrow} + \lambda \end{pmatrix} \quad (6)$$

The local Skyrme p-h Hamiltonian h has the usual form [7, 8]:

$$h_q(\mathbf{r}, \sigma, \sigma') = -\nabla \cdot \frac{\hbar^2}{2m^*} \nabla + U_q - i\mathbf{B}_q \cdot (\nabla \times \sigma) \quad (7)$$

where m^* is the effective mass, U_q is the central p-h mean-field potential including the Coulomb term for protons, and the spin-orbit potential with

$$\mathbf{B}_q = \frac{1}{2}W_q(\nabla\rho(\mathbf{r}) + \nabla\rho_q(\mathbf{r})), \quad (8)$$

where W_q is the spin-orbit coupling strength.

The pairing Hamiltonian \tilde{h} corresponding to the zero-range density-dependent δ interaction can be written as

$$\tilde{h}_q(\mathbf{r}, \sigma, \sigma') = V_0^q \tilde{\rho}_q(\mathbf{r}) F(\mathbf{r}) \delta_{\sigma\sigma'} \quad (9)$$

where $V_0^q < 0$ is the pairing strength, and the pairing form factor $F(\mathbf{r})$ depends on the form of pairing Hamiltonian [22]:

$$F(\mathbf{r}) = \begin{cases} 1 & \text{-- volume pairing} \\ 1 - \frac{\rho(\mathbf{r})}{\rho_0} & \text{-- surface pairing} \\ 1 - \frac{\rho(\mathbf{r})}{2\rho_0} & \text{-- mixed pairing} \end{cases} \quad (10)$$

where $\rho_0=0.16 \text{ fm}^{-3}$. The volume pairing interaction acts primarily inside the nuclear volume while the surface pairing generates pairing fields peaked around or outside the nuclear surface. As discussed in Ref. [23], different forms of $F(\mathbf{r})$ can result in notable differences of pairing fields in diffused drip-line nuclei.

B. B-spline technique in HFB-AX

The lattice representation of wave functions and the HFB Hamiltonian used in this work closely follows that of HFB-2D-LATTICE described in Ref. [16]. In HFB-AX, the wave functions are discretized on a 2D grid (r_α, z_β) with the M -order B-splines:

$$\psi_{n\Omega^\pi q}^{(1,2)}(\rho_\alpha, z_\beta) = \sum_{i,j} B_i^M(\rho_\alpha) B_j^M(z_\beta) C_{n\Omega^\pi q}^{ij(1,2)}, \quad (11)$$

where C^{ij} is the matrix of expansion coefficients; $\alpha = 1, \dots, N_\rho$ and $\beta = 1, \dots, N_z$. The four components of HFB wave functions (2) are thus represented in a matrix form. The derivative operators are constructed using the Galerkin method. In the B-spline representation, the HFB Hamiltonian acts on 2D wave functions like a tensor, i.e.,

$$h_{\gamma\delta}^{\alpha\beta} \psi(\rho_\alpha, z_\beta) = \psi'(\rho_\gamma, z_\delta). \quad (12)$$

The HFB equation is solved by mapping the Hamiltonian tensor into a matrix, which is then diagonalized. The

associated wave functions $\langle \Psi^* |$ and $|\Psi\rangle$ are mapped into the bra and ket vectors, respectively:

$$\langle \Psi_{\gamma\delta}^* | \mathcal{H}_{\gamma\delta}^{\alpha\beta} | \Psi_{\alpha\beta} \rangle = E. \quad (13)$$

In the following, we give some details pertaining to the Hamiltonian mapping, because the mapping rule is different with respect to the 16 individual blocks in Eq. (6). For the diagonal blocks, it is straightforward to map a tensor into a matrix (k, k'):

$$\begin{aligned} h(\uparrow\uparrow) : & \begin{cases} k = (\beta - 1)N_\rho + \alpha \\ k' = (\delta - 1)N_\rho + \gamma \end{cases} \\ h(\downarrow\downarrow) : & \begin{cases} k = (\beta - 1)N_\rho + \alpha + N_\rho N_z \\ k' = (\delta - 1)N_\rho + \gamma + N_\rho N_z \end{cases} \\ -h(\uparrow\downarrow) : & \begin{cases} k = (\beta - 1)N_\rho + \alpha + 2 \times N_\rho N_z \\ k' = (\delta - 1)N_\rho + \gamma + 2 \times N_\rho N_z \end{cases} \\ -h(\downarrow\uparrow) : & \begin{cases} k = (\beta - 1)N_\rho + \alpha + 3 \times N_\rho N_z \\ k' = (\delta - 1)N_\rho + \gamma + 3 \times N_\rho N_z \end{cases} \end{aligned} \quad (14)$$

Following the same rule, the bra and ket vectors are mapped into vectors with indexes k and k' , respectively. It is more complicated to map the off-diagonal blocks of (6). For the four ket vectors, the mapped index k should correspond to different columns of the Hamiltonian blocks. For example, the index of the first ket component $U^{(1)}$ should correspond to the upper index of the first column of (6):

$$(U^{(1)*} \ D^{(1)*} \ U^{(2)*} \ D^{(2)*}) \begin{pmatrix} \overline{h^{\alpha\beta}(\uparrow\uparrow)} - \lambda & h(\uparrow\downarrow) & \tilde{h}(\uparrow\uparrow) & \tilde{h}(\uparrow\downarrow) \\ h^{\alpha\beta}(\downarrow\uparrow) & h(\downarrow\downarrow) - \lambda & \tilde{h}(\downarrow\uparrow) & \tilde{h}(\downarrow\downarrow) \\ \tilde{h}^{\alpha\beta}(\uparrow\uparrow) & \tilde{h}(\uparrow\downarrow) & -h(\uparrow\uparrow) + \lambda & -h(\uparrow\downarrow) \\ \tilde{h}^{\alpha\beta}(\downarrow\uparrow) & \tilde{h}(\downarrow\downarrow) & -h(\downarrow\uparrow) & -h(\downarrow\downarrow) + \lambda \end{pmatrix} \begin{pmatrix} \overline{U^{(1)}(\rho_\alpha z_\beta)} \\ D^{(1)} \\ U^{(2)} \\ D^{(2)} \end{pmatrix}. \quad (15)$$

For the four bra vectors, the mapped index k' corresponds to different rows of the Hamiltonian. For example, the index of the first bra component $U^{(1)*}$ corresponds to the lower index of the first row of (6):

$$\begin{pmatrix} \overline{|U^{(1)*}(\rho_\gamma z_\delta)|} & D^{(1)*} & U^{(2)*} & D^{(2)*} \end{pmatrix} \begin{pmatrix} h_{\gamma\delta}(\uparrow\uparrow) - \lambda & h_{\gamma\delta}(\uparrow\downarrow) & \tilde{h}_{\gamma\delta}(\uparrow\uparrow) & \tilde{h}_{\gamma\delta}(\uparrow\downarrow) \\ h(\downarrow\uparrow) & h(\downarrow\downarrow) - \lambda & \tilde{h}(\downarrow\uparrow) & \tilde{h}(\downarrow\downarrow) \\ \tilde{h}(\uparrow\uparrow) & \tilde{h}(\uparrow\downarrow) & -h(\uparrow\uparrow) + \lambda & -h(\uparrow\downarrow) \\ \tilde{h}(\downarrow\uparrow) & \tilde{h}(\downarrow\downarrow) & -h(\downarrow\uparrow) & -h(\downarrow\downarrow) + \lambda \end{pmatrix} \begin{pmatrix} U^{(1)} \\ D^{(1)} \\ U^{(2)} \\ D^{(2)} \end{pmatrix}. \quad (16)$$

Following this scheme, the HFB Hamiltonian, represented by 16 tensor blocks, is mapped into a matrix of the rank $4 \times N_\rho N_z$. The resulting HFB Hamiltonian matrix is diagonalized using LAPACK routines [24].

The Coulomb potential is obtained by directly integrating the Poisson equation,

$$\nabla^2 \phi(\rho, z) = -4\pi e^2 \rho_p(\rho, z), \quad (17)$$

where ϕ is the Coulomb potential and ρ_p is the proton density. The Poisson equation, discretized on a B-spline grid, can be written in a matrix form. The boundary conditions at large distances are given by the multipole expansion of the Coulomb potential [16]. The gradient of the Coulomb potential at $z=0$ or $\rho=0$ is set to be zero be-

cause of the symmetries imposed. These boundary conditions are incorporated in the lattice representation of the Laplace operator.

C. Numerical speedup

The size of the HFB Hamiltonian matrix depends on the box size R , the largest distance between neighboring mesh points in the grid h (the B-spline grid is not

uniform), and the order of B-splines M . Consequently, for large and refined grids, the diagonalization time becomes a bottleneck. For example, for ^{120}Sn with a box of 19.2 fm, a maximum grid size of $h=0.6$ fm, and $M=13$, the Hamiltonian matrix is about 0.45 GB of storage, and one diagonalization takes about 30 CPU minutes.

Since the diagonalization of HFB matrices corresponding to different Ω^π blocks can be done independently, this part of HFB-AX can be parallelized using the Message Passing Interface. For ^{120}Sn with $\Omega_{\text{max}}=33/2$ cutoff, about 70 processors are utilized. The precision of the derivative operators is crucial for the accuracy of the HFB eigenstates. By distributing diagonalization over many processors, one can perform calculations with larger boxes, denser grids, and higher-order B-splines. In addition, by taking advantage of the reflection symmetry, N_z can be reduced; hence the rank of the Hamiltonian matrix is scaled down by a factor slightly less than 2. Consequently, the diagonalization process, which takes most of the execution time, can be speeded up by a factor greater than 8.

For the diagonalization, we employ the LAPACK DGEEV routine [24]. This routine diagonalizes a non-symmetric matrix using a QR algorithm. However, due to energy cutoff in HFB, it is not necessary to compute all eigenvectors. For this reason, we modified DGEEV so that it yields eigenvectors only within the required energy window. By this way, the diagonalization time for ^{120}Sn is further reduced by one-third.

To optimize the convergence of HFB iterations, we take the HF-BCS densities to warm-start the self-consistent process. Furthermore, instead of the commonly used linear mixing, we have implemented the modified Broyden mixing, quasi-Newton algorithm to solve large sets of non-linear equations, for accelerating the convergence rate [25]. The iterative convergence can be estimated by the input and output difference at the m -th iteration,

$$\mathbf{F}^{(m)} = \mathbf{V}_{\text{out}}^{(m)} - \mathbf{V}_{\text{in}}^{(m)}, \quad (18)$$

where \mathbf{V} is an N -dimensional vector containing unknowns, and self-consistency condition requires that the solution \mathbf{V}^* be a fixed-point of the iteration: $\mathbf{I}(\mathbf{V}^*) = \mathbf{V}^*$. For the linear mixing, the input at iteration $m+1$ is given as

$$\mathbf{V}_{\text{in}}^{(m+1)} = \mathbf{V}_{\text{in}}^{(m)} + \alpha \mathbf{F}^{(m)}, \quad (19)$$

where α is a constant between 0 and 1. In contrast, to estimate the next step, the modified Broyden mixing utilizes information obtained in previous M_B iterations. Recent implementations of this technique to the HFB problem have demonstrated that the sufficient convergence can generally be obtained within 20-30 iterations [26]. In HFB-AX the vector \mathbf{V} consists of local densities and their derivatives at lattice mesh points:

$$\mathbf{V} \equiv \{\rho_q, \tau_q, \nabla \cdot \mathbf{J}_q, \tilde{\rho}_q, \nabla^2 \rho_q, \nabla_\rho \rho_q, \nabla_z \rho_q\}. \quad (20)$$

The dimension of \mathbf{V} is thus $14 \times N_\rho \times N_z$.

To demonstrate the performance of the method, we consider ^{22}O in a 2D square box of $R=12$ fm, $h=0.6$ fm and $M=11$. The calculations were carried out on a Cray XT3 supercomputer at ORNL having 2.6 GHz AMD processors. Without reflection symmetry, one diagonalization takes about 15 minutes of CPU time. With reflection symmetry imposed, one diagonalization needs about 100 seconds with the modified DGEEV. The calculations with Broyden's mixing with $M_B=7$ are displayed in Fig. 1. The actual variation of binding energy is within 0.1 keV after 30 iterations. This is to be compared with linear mixing with $\alpha=0.6$ which requires over 80 iterations to reach similar convergence. Both calculations show precision limitations due to the numerical noise inherent to the mesh assumed. As in examples discussed in Ref. [26], Broyden's method implemented in HFB-AX provides impressive performance improvements of HFB iterations. The numerical speedup is particularly helpful for heavy nuclei and for constrained calculations, which usually require many self-consistent iterations.

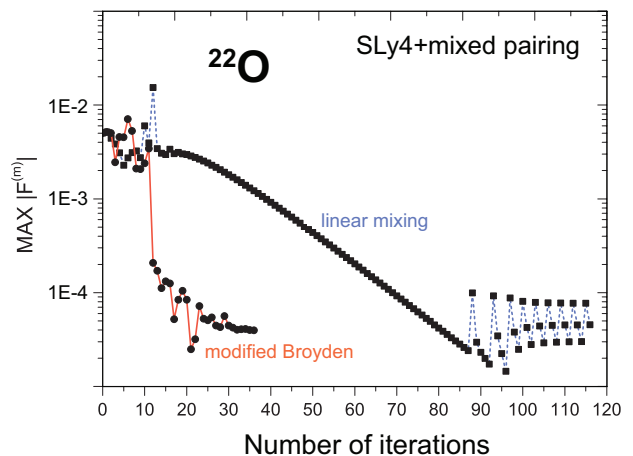


FIG. 1: (Color online) Comparison between linear mixing (squares) and modified Broyden's method (circles) in HFB-AX for ^{22}O . The largest element of $|\mathbf{F}^{(m)}|$ is shown as a function of the number of iterations m . See text for details.

III. BENCHMARKING OF HFB-AX AND TYPICAL APPLICATIONS

This section contains results of HFB-AX test results. First, the absolute accuracy of the one-body HF solver is tested using the adaptive multi-resolution method. Thereafter follows a series of calculations in which HFB-AX is benchmarked against the spherical coordinate space code HFBRAD and the axial code HFBTHO. In all those realistic tests, the Skyrme functional SLy4 [27] was used in the p-h channel, augmented by different density-dependent delta functionals (9) in the p-p channel.

A. Two-center potential: comparison with HO and wavelet expansions

The accuracy of the HFB-AX calculations in the p-h channel has been tested using an adaptive multiwavelet basis. To this end, we employed the MADNESS framework [17]. The details regarding our particular realization of the wavelet basis expansion can be found in Refs. [18, 28].

As a test case, we choose an axial two-center inverted-cosh potential:

$$V(\rho, z) = V_0 [f(\rho, z + \zeta) + f(\rho, z - \zeta)], \quad (21)$$

where the inverted-cosh form factor is:

$$f(\rho, z) = \frac{1}{1 + e^{-R_0/a} \cosh(\sqrt{\rho^2 + z^2}/a)}, \quad (22)$$

and V_0 , R_0 , and a are the potential's depth, radius, and diffuseness, respectively, and 2ζ is the distance between the two centers. A cross section of the potential used in our test calculations is shown in Fig. 2 along the z -axis at $\rho=0$. It is seen that the two potential's centers are well separated; hence the ability to predict a small parity splitting between the eigenstate doublets provides a stringent test for the B-spline Schrödinger equation solver of HFB-AX.

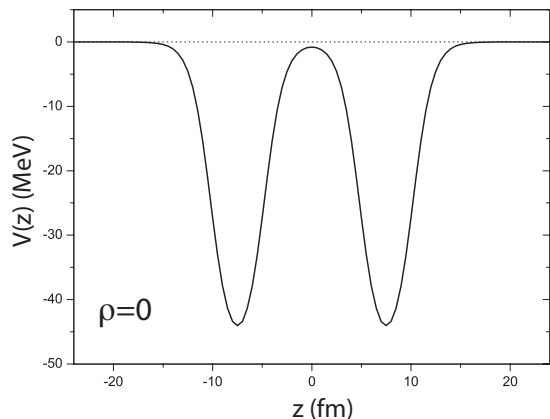


FIG. 2: The two-center inverted-cosh potential of Eq. (21) as a function of z at $\rho=0$. The two centers are 15 fm apart ($\zeta=7.5$ fm) and $V_0=-50$ MeV, $R_0=2$ fm, and $a=1$ fm.

In addition to potential (21) we also considered the spin-orbit term in the usual Thomas form:

$$V_{SO}(\rho, z) = -i\lambda_0 \left(\frac{\hbar}{2mc} \right)^2 \nabla V(\rho, z) \cdot (\boldsymbol{\sigma} \times \nabla), \quad (23)$$

where $\lambda_0=5.0$ and the numerical values of fundamental constants were taken as $\hbar^2/2m=20.721246$ fm², $\hbar c=197.32696$ MeV fm, and $mc^2=939.56535$ MeV. The

corresponding one-body Schrödinger equation reads:

$$\left[-\frac{\hbar^2}{2m} \nabla^2 + V(\rho, z) + V_{SO}(\rho, z) \right] \varphi(\rho, z, \phi) = E \varphi(\rho, z, \phi), \quad (24)$$

where $\varphi(\rho, z, \phi)$ is a two-component spinor wave function.

TABLE II: Ten lowest eigenvalues of the two-center potential (21) obtained using the HO, B-spline, and wavelet expansions. All energies are in MeV. For more details see text.

State No.	Ω^π	HO	HO	B-spline	Wavelets
		$N_{sh}=20$	$N_{sh}=30$	$h=0.6$	
1	$1/2^+$	-22.23916	-22.24008	-22.24011	-22.24011
2	$1/2^-$	-22.23816	-22.23995	-22.23998	-22.23998
3	$1/2^+$	-9.21514	-9.22047	-9.22050	-9.22050
4	$3/2^-$	-9.20359	-9.21256	-9.21260	-9.21260
5	$1/2^-$	-9.20359	-9.21256	-9.21260	-9.21260
6	$3/2^+$	-9.20589	-9.21126	-9.21129	-9.21129
7	$1/2^+$	-9.20589	-9.21126	-9.21129	-9.21129
8	$1/2^-$	-9.19743	-9.20590	-9.20595	-9.20595
9	$1/2^+$	-1.70724	-1.72402	-1.72503	-1.72514
10	$1/2^-$	-1.49218	-1.52486	-1.52672	-1.52690

Table II displays the lowest eigenvalues of the two-center potential (21) obtained in three expansion methods. In the HO expansion calculation, we took $N_{sh}=20$ and 30 shells of the spherical oscillator with $\hbar\omega_0=5.125$ MeV (as it turned out, the use of a stretched basis was not particularly advantageous). The size of the $\Omega^\pi=\frac{1}{2}^+$ Hamiltonian block is 121 and 256 for $N_{sh}=20$ and 30, respectively, i.e., the matrix size is more than doubled in the latter case. In the HFB-AX calculation with $M=13$, we used a square box of $R=25.2$ fm and $h=0.6$ fm. (The values of $N_{sh}=20$ in HO and $h=0.6$ fm in HFB-AX are typical for realistic Skyrme-HFB calculations.) In the wavelet variant [18, 28], the absolute accuracy was assumed to be 10^{-5} .

It is seen that the accuracy of B-spline expansion is excellent, both for the absolute energies and for the parity splitting. The HO basis with $N_{sh}=20$ performs rather poorly, especially for parity splitting and for the energies of the highest (halo) states. That is, of course, to be expected for a two-center potential expanded in a one-center basis. It is only at $N_{sh}=30$, not practical in large-scale DFT calculations, that a good agreement with wavelets and HFB-AX is obtained. In all variants, there is a perfect degeneracy of $p_{3/2}$ doublets with $\Omega=\frac{1}{2}$ and $\Omega=\frac{3}{2}$.

The results with the inclusion of the spin-orbit term, which lifts the degeneracy between $\Omega=\frac{1}{2}$ and $\frac{3}{2}$ levels, are given in Table III. It is seen that the general excellent agreement between B-spline and wavelet variants holds, and that HO with $N_{sh}=20$ performs rather poorly, especially for the halo state. Finally, the single-particle spectrum of a two-center potential is illustrated in Fig. 3 as a function of the inter-center distance. A transition to a dimer-like spectrum is clearly seen at distances greater

TABLE III: Similar to Table II except for the two-center double-cosh potential with the spin-orbit term.

State No.	Ω^π	HO	HO	B-spline	Wavelets
		$N_{sh}=20$	$N_{sh}=30$	$h=0.6$	
1	$1/2^+$	-22.23916	-22.24008	-22.24011	-22.24011
2	$1/2^-$	-22.23816	-22.23995	-22.23998	-22.23998
3	$1/2^+$	-9.43145	-9.43659	-9.43663	-9.43662
4	$3/2^-$	-9.42314	-9.43199	-9.43203	-9.43202
5	$3/2^+$	-9.42561	-9.43078	-9.43081	-9.43080
6	$1/2^-$	-9.41931	-9.42783	-9.42788	-9.42788
7	$1/2^+$	-8.77250	-8.77825	-8.77828	-8.77828
8	$1/2^-$	-8.76475	-8.77380	-8.77384	-8.77383
9	$1/2^+$	-1.70727	-1.72405	-1.72506	-1.72516
10	$1/2^-$	-1.49222	-1.52490	-1.52675	-1.52693

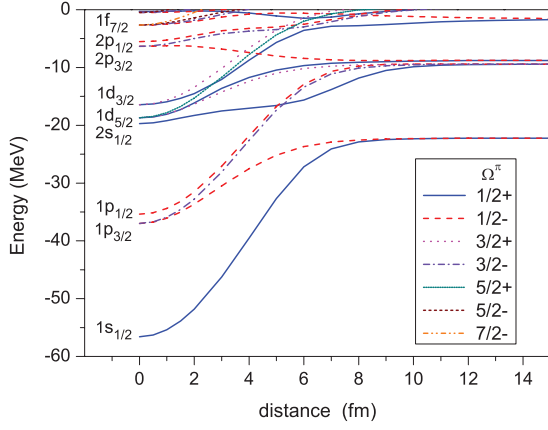


FIG. 3: (Color online) Eigenvalues of a two-center inverted-cosh potential with the spin-orbit term calculated in HFB-AX as functions of the distance between two centers 2ζ .

than 6 fm. Our tests nicely illustrate the ability of the B-spline technique (thus: HFB-AX) to handle a two-center problem encountered, e.g., in fission or fusion [29].

B. Spherical limit: comparison with HFBRAD and HFBTHO

The performance of HFB-AX at the spherical limit can be assessed by comparing it against the accurate 1D radial coordinate code HFBRAD, based on a direct integration of the system of coupled radial differential equations [7, 13]. The tests have been carried out for the nucleus ^{120}Sn , which is often used in benchmarking HFB solvers [16, 20] in the limit of spherical shape and nonzero neutron pairing.

The precision of HFB calculations in coordinate space is primarily determined by the size of the mesh used. We calculated ^{120}Sn with the fixed-box size ($R=19.2$ fm) but with different mesh steps and B-spline orders. In our calculations, we took the volume delta pairing interaction with the pairing strength $V_0=-187.05$ MeV fm³ adjusted to the experimental neutron pairing gap of $\Delta_n=1.245$

MeV. For the pairing space, we adopted the commonly used equivalent energy cutoff of 60 MeV [20]. As both codes are written in different geometry, the quasiparticle continuum is discretized differently in HFBRAD and HFB-AX. In HFBRAD, all partial waves with $j \leq j_{\text{max}}=33/2$ were considered, while in HFB-AX we imposed a cutoff on j_z : $\Omega_{\text{max}}=33/2$. For the sake of comparison, the pairing regularization option in HFBRAD has been turned off. Also, we adopted the same fundamental constants as in Ref [20]: $\hbar^2/2m = 20.73553$ MeV and $e^2=1.439978$ MeV fm.

TABLE IV: Results of spherical HFB+SLy4 calculations with volume pairing for ^{120}Sn using HFB-AX with different mesh size h and B-spline order M . The results of the precision radial code HFBRAD are shown for comparison. The static proton pairing is zero. All energies are in MeV; h is in fm.

E	$h=0.64$	$h=0.6$	$h=0.6$	$h=0.15$
	$M=11$	$M=11$	$M=13$	HFBRAD
E_{tot}	-1018.304	-1018.271	-1018.356	-1018.362
E_C	347.636	347.642	347.577	347.558
E_{kin}^p	831.520	831.512	831.534	831.520
E_{kin}^n	1339.516	1339.553	1339.562	1339.598
E_{pair}^n	-10.253	-10.253	-10.253	-10.278
\tilde{E}_{kin}^n	1329.263	1329.300	1329.309	1329.320
Δ_n	1.2451	1.2451	1.2451	1.2450
λ_n	-7.9950	-7.9950	-7.9950	-7.9953

Table IV displays various contributions to the binding energy E_{tot} of ^{120}Sn , i.e., kinetic energy E_{kin} for protons and neutrons, Coulomb energy E_C , neutron pairing energy E_{pair}^n , neutron pairing gap Δ_n and Fermi level λ_n , and the sum

$$\tilde{E}_{\text{kin}} = E_{\text{kin}} + E_{\text{pair}} \quad (25)$$

for neutrons. (As discussed in Refs. [30, 31, 32], while for zero-range pairing the individual values of E_{kin} and E_{pair} are divergent with respect to the cutoff energy of the pairing window, their sum (25) converges nicely and it is less sensitive to the actual treatment of discretized quasiparticle continuum.) The general agreement between HFB-AX and HFBRAD is excellent, in particular in the $h=0.6$ fm, $M=13$ variant, with most quantities agreeing within 10 keV. As expected, the largest difference is seen for E_{kin}^n and E_{pair}^n due to a slightly different character of unbound spectrum in the two models; however, the sum \tilde{E}_{kin} is well reproduced by HFB-AX.

The HFB results with mixed pairing obtained in HFB-AX, HFBRAD, and HFBTHO are shown in Table V. The pairing strength in HFB-AX was taken as $V_0=-284.29$ MeV fm³, as compared to -284.36 and -284.10 MeV fm³ in HFBRAD and HFBTHO, respectively [20]. In HFBTHO calculations, 25 shells of transformed HO basis were used. Again, the agreement between HFB-AX and HFBRAD is excellent, and the total binding energies obtained in the three methods agree within 12 keV. As expected, the largest differences are seen for E_{kin} . In par-

TABLE V: Similar to Table IV except for the mixed pairing interaction. HFB-AX results are compared with those of HFBRAD and HFBTHO of Ref. [20].

E	$h=0.6$ $M=13$	$h=0.1$ HFBRAD	HFBTHO
E_{tot}	-1018.795	-1018.791	-1018.777
E_C	347.442	347.400	347.370
E_{kin}^p	830.856	830.848	830.735
E_{kin}^n	1340.675	1340.668	1340.458
E_{pair}^n	-12.491	-12.467	-12.467
E_{kin}^n	1328.184	1328.201	1327.991
Δ_n	1.2448	1.2446	1.2447
λ_n	-8.0186	-8.0181	-8.0168

ticular, HFBTHO underestimates the neutron (proton) kinetic energy by about 200 (100) keV. This deviation is partly due to different representations of the kinetic energy operator in the coordinate space and in the transformed oscillator basis, and partly due to the different continuum space (see the discussion above).

C. Weak binding regime: comparison with HFBRAD

Neutron-rich nuclei are unique laboratories of neutron pairing. In weakly bound nuclei, pairing fields are affected by the coupling to the continuum space, and this coupling can significantly modify pair distributions [8, 23, 33, 34]. In Sec. III B we demonstrated that HFB-AX performs very well for a stable spherical nucleus ^{120}Sn . To evaluate the performance of HFB-AX for weakly bound nuclei, in this section we discuss ground-state properties of even-even $^{84,86,88,90}\text{Ni}$ isotopes, which are expected to be weakly bound [10, 35, 36, 37].

In our test calculations, we adopted the surface pairing with strength adjusted to ^{120}Sn ($V_0 = -512.6 \text{ MeV fm}^3$). Results of HFBRAD and HFB-AX calculations are listed in Table VI. The nucleus ^{90}Ni is a drip-line system and its stability is strongly influenced by pairing. Indeed, it is only bound with surface pairing; with volume and mixed pairing, ^{90}Ni is calculated to have a positive neutron chemical potential (see Ref. [23] for more discussion concerning this point). The local particle and pairing densities of drip-line even-even Ni isotopes are shown in Fig. 4. A gradual increase of neutron skin as approaching ^{90}Ni is clearly seen. The proton density, on the other hand, is only weakly affected by the outermost neutrons.

The systematic comparison between HFB-AX and HFBRAD is given in Table VI. For the binding energy, the agreement is very good, including the borderline system ^{90}Ni . The neutron pairing energy increases as one approaches the neutron drip line. This is consistent with the systematic behavior of pairing densities shown in Fig. 4.

For ^{84}Ni , HFB-AX and HFBRAD yield similar pairing properties and kinetic energies. However, with increas-

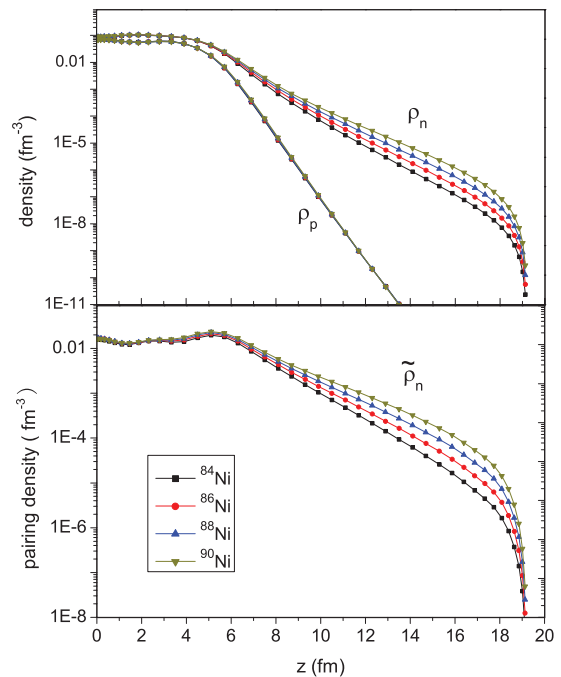


FIG. 4: (Color online) Proton (top) and neutron pairing (bottom) densities calculated in HFB-AX for $^{84,86,88,90}\text{Ni}$. Proton pairing is zero.

ing neutron number, the difference between the values of \tilde{E}_{kin}^n obtained in the two models gradually grows, reaching over 1.6 MeV in ^{90}Ni . At the same time, the difference between E_{kin}^p values is smaller by an order of magnitude. The systematic difference between HFB-AX and HFBRAD when approaching the neutron drip line can be traced back to different angular momentum truncations, i.e., pairing phase space structure. In HFBRAD, the s.p. angular momentum cutoff is $j_{\max}=33/2$, while in the HFB-AX, the cutoff is done in terms of the s.p. angular momentum projection and it is $\Omega_{\max}=33/2$. Consequently, in HFB-AX contributions from high- j , low- Ω continuum states, absent in HFBRAD, are present. In Sec. III B, we have shown that for the well-bound nucleus ^{120}Sn , this difference in the continuum phase space is insignificant. However, for nuclei close to the drip line, where the contribution from unbound states is far more important, the situation is very different.

In order to quantify this point, we performed calculations for ^{90}Ni with $j_{\max}=49/2$ in HFBRAD and $\Omega_{\max}=49/2$ in HFB-AX. The results are displayed in Table VII. The variations in the proton kinetic energy between various variants of calculations are small, suggesting that the kinetic energy operator is well represented by HFBRAD and HFB-AX with the grids assumed. Also, the binding energy changes little, $\sim 30 \text{ keV}$, when the j - or Ω -cutoff is increased. In the larger j -window, \tilde{E}_{kin}^n in HFBRAD is reduced by about 1 MeV; the corresponding change in HFB-AX is much smaller, $\sim 200 \text{ keV}$. This result indicates that the high- j continuum contributions play an important role in the structure of ^{90}Ni . A need for an

TABLE VI: Comparison between HFB-AX and HFBRAD with SLy4 p-h functional and surface pairing for drip-line nuclei $^{84,86,88,90}\text{Ni}$. The same box $R=19.2\text{ fm}$ was used in both cases. The angular momentum cutoff was taken at $j_{\text{max}}=33/2$ in HFBRAD and $\Omega_{\text{max}}=33/2$ in HFB-AX. All energies are in MeV.

	^{84}Ni		^{86}Ni		^{88}Ni		^{90}Ni	
E	HFBRAD	HFB-AX	HFBRAD	HFB-AX	HFBRAD	HFB-AX	HFBRAD	HFB-AX
E_{tot}	-654.919	-654.899	-656.915	-656.955	-658.215	-658.193	-658.877	-658.856
E_C	122.797	122.806	122.215	122.228	121.621	121.640	121.018	121.056
E_{kin}^p	430.468	430.460	426.311	426.330	422.152	422.206	418.027	418.204
E_{kin}^n	1084.511	1084.577	1116.835	1116.782	1148.387	1148.179	1179.697	1178.956
E_{pair}^n	-30.892	-30.890	-36.733	-37.080	-43.179	-43.727	-49.926	-50.807
\tilde{E}_{kin}^n	1053.619	1053.687	1080.102	1079.702	1105.208	1104.452	1129.771	1128.149
Δ_n	1.485	1.486	1.613	1.617	1.742	1.746	1.862	1.864
λ_n	-1.455	-1.454	-1.062	-1.068	-0.709	-0.718	-0.399	-0.417

TABLE VII: Similar to Table VI except for ^{90}Ni with the angular momentum cutoff $j_{\text{max}}=49/2$ in HFBRAD and $\Omega_{\text{max}}=49/2$ in HFB-AX. All energies are in MeV.

	HFBRAD	HFB-AX
E_{tot}	-658.911	-658.881
E_C	121.038	121.060
E_{kin}^p	418.165	418.233
E_{kin}^n	1179.073	1178.843
E_{pair}^n	-50.326	-50.892
\tilde{E}_{kin}^n	1128.747	1127.951
Δ_n	1.860	1.864
λ_n	-0.410	-0.420

appreciable angular momentum cutoff in the description of weakly bound nuclei, especially for surface-like pairing interactions, has been pointed out in Ref. [38].

D. Deformed, weakly bound case: comparison with HFBTHO

One of the objectives of HFB-AX is to precisely solve HFB equations for axially deformed nuclei, in particular at very large deformations and/or at the limit of weak binding. In this context, the neutron-rich Zr isotopes with $A \sim 110$ are very useful testing grounds, as they are known to have very large prolate deformations [16]. In this section, we compare axial HFB-AX and HFBTHO calculations for the nuclei $^{102,110}\text{Zr}$ which exhibit deformed neutron skin.

Table VIII shows the results of deformed calculations for ^{102}Zr and ^{110}Zr with the same parameters as in spherical calculations for ^{120}Sn displayed in Table V. In HFBTHO, deformed wave functions were expanded in the space of 20 stretched HO shells. The binding energies in HFB-AX are greater by about 110-140 keV than those of HFBTHO. This is understandable as HFBTHO with 20 shells also underestimates the binding energy of ^{120}Sn by about 150 keV [20]. In Table VIII we only show neutron pairing (proton pairing correlations in ^{110}Zr vanish due to a deformed proton subclosure at $Z=40$). It is grat-

TABLE VIII: Results of deformed HFB-AX and HFBTHO HFB+SLy4 calculations for ^{102}Zr and ^{110}Zr with mixed pairing. All energies are in MeV. The quadrupole moments are in fm^2 .

	^{102}Zr		^{110}Zr	
	HFB-AX	HFBTHO	HFB-AX	HFBTHO
E_{tot}	-859.649	-859.540	-893.983	-893.840
E_C	231.149	231.084	226.758	226.712
E_{kin}^p	651.309	651.099	632.115	631.882
E_{kin}^n	1202.050	1201.990	1368.206	1368.201
E_{pair}^n	-3.261	-3.535	-3.200	-3.323
\tilde{E}_{kin}^n	1198.789	1198.455	1365.006	1364.878
Δ_n	0.672	0.700	0.636	0.652
λ_n	-5.431	-5.435	-3.552	-3.543
Q_{20}^p	410.08	411.31	444.02	443.90
Q_{20}^n	638.19	639.41	788.32	786.63

ifying to see that energies and quadrupole moments of ^{102}Zr and ^{110}Zr are very close in HFB-AX and HFBTHO, in spite of fairly different computational strategies underlying these two codes.

TABLE IX: Comparison between HFB-2D-LATTICE (second column) and HFB-AX (third column) for ^{102}Zr . Calculation parameters are the same as in Ref. [14], i.e., $V_0=-170\text{ MeV fm}^3$, $\Omega_{\text{max}}=11/2$, $R=12\text{ fm}$, and $N_p=N_z=19$. The results of HFB-AX with the same density functional but the standard box $R=19.2\text{ fm}$ and larger pairing cutoff $\Omega_{\text{max}}=33/2$ are displayed in the last column (HFB-AX'). All energies are in MeV. The mass rms radius R_{rms} is in fm.

	HFB-2D-LATTICE	HFB-AX	HFB-AX'
E_{tot}	-859.61	-859.19	-859.25
λ_n	-5.46	-5.47	-5.45
λ_p	-12.10	-12.05	-12.06
Δ_n	0.31	0.28	0.43
Δ_p	0.34	0.37	0.40
R_{rms}	4.58	4.58	4.58
β_2	0.431	0.434	0.435

In order to compare HFB-AX with the Vanderbilt lattice code HFB-2D-LATTICE, we calculated the deformed nu-

cleus ^{102}Zr assuming the same parameters as in Ref. [14], i.e., a fairly small box radius $R=12$ fm, coarse grid, and very low cutoff $\Omega_{\text{max}}=11/2$. The ground state of ^{102}Zr is reflection symmetric; thus, apart from the fact that the box of HFB-2D-LATTICE is twice as large as that of HFB-AX, the codes are supposed to produce the same result. As seen in Table IX, this is almost the case: the difference for the binding energy is around 400 keV. We believe that this can be attributed to a slightly different structure of the discretized positive-energy continuum in the two codes. Indeed the average pairing gaps predicted in the two codes are ~ 30 keV apart. To confirm this, we performed another calculation for ^{102}Zr in a larger space, i.e., $R=19.2$ fm, $h=0.6$ fm, and $\Omega_{\text{max}}=33/2$. While the total energy is only weakly affected, there is an appreciable increase in the pairing gaps. This result, together with the discussion of ^{90}Ni in Sec. III C, underlines the importance of using large boxes and sizable pairing spaces for the description of neutron-rich systems.

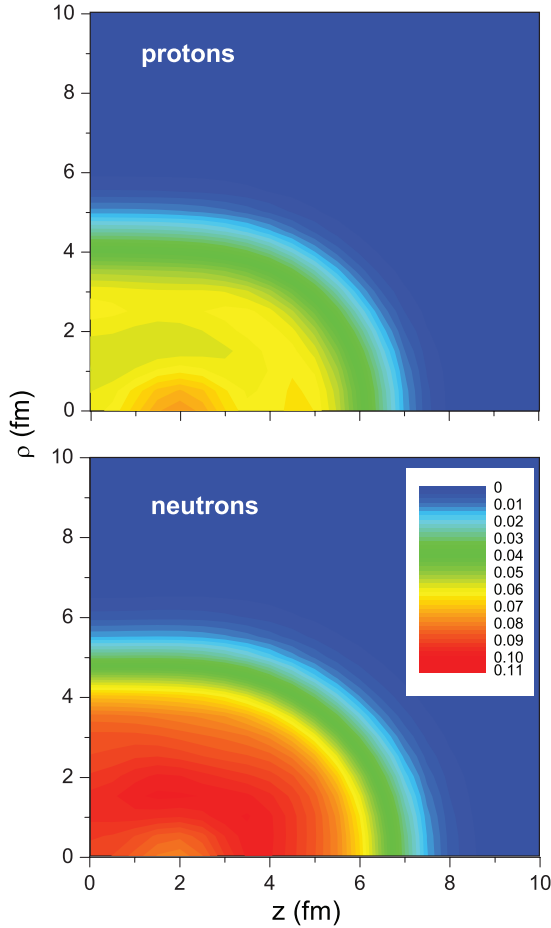


FIG. 5: (Color online) Contour plots of proton (top) and neutron (bottom) density distributions in the (ρ, z) -plane for the deformed ground state of ^{110}Zr calculated in HFB-AX. The densities are in nucleons/ fm^{-3} .

Proton and neutron density distributions in ^{110}Zr are displayed in Figs. 5 (in two dimensions, to better show

the deformed shape) and 6 (in logarithmic scale, to better show the asymptotic behavior). The appearance of the neutron skin beyond the nuclear surface is clearly seen. The density contours in Fig. 5 can be compared with the result of HFB-2D-LATTICE shown in Fig. 6 of Ref. [16], and there seems to appear a good agreement between the two sets of calculations. In particular, a small depression of density in the nuclear interior, due to shell effects, is present in both cases. Another interesting feature is the constancy of density diffuseness along the nuclear surface. The asymptotic behavior of nuclear den-

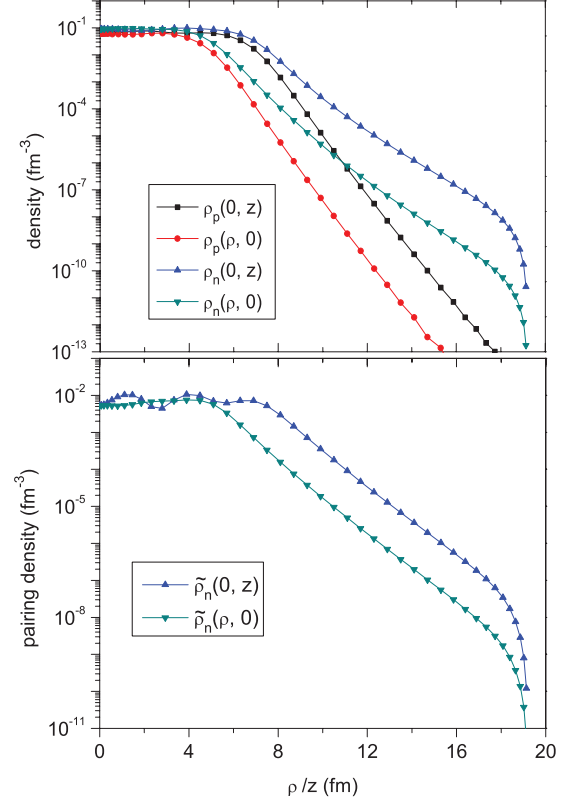


FIG. 6: (Color online) Particle (top) and pairing (bottom) ground-state densities in ^{110}Zr along $\rho=0$ and $z=0$. The size of the box is $R=19.2$ fm.

sities in Fig. 6 is consistent with general expectations [8], and the ratio $\rho_n(0, z)/\rho_n(\rho = z, 0)$ is roughly constant at large distances. This indicates that densities are still well deformed in the region which is well beyond the nuclear surface.

E. Large deformation limit: axial symmetric fission path of ^{240}Pu

The advantage of coordinate-space calculations over HO expansion methods is apparent in the context of problems involving extreme deformations, which require the use of huge oscillator spaces or even a many-center HO basis. In this section, we study the axial, reflection-

symmetric fission path of ^{240}Pu , which has been investigated in many earlier works [4]. By carrying out precise HFB-AX calculations, one can assess the error on potential energy surfaces, energies of fission isomers, and fission barriers obtained in commonly used HFB codes employing an HO expansion technique.

The HFB energy at a given mass quadrupole moment $Q_{20} = \langle \hat{Q}_{20} \rangle$ can be obtained by minimizing the routhian with a quadratic constraint [19]:

$$E' = E + C_q (\langle \hat{Q}_{20} \rangle - Q_{20})^2 \quad (26)$$

where

$$Q_{20} = 2\pi \int \int \rho_{\text{tot}}(\rho, z) (2z^2 - \rho^2) \rho d\rho dz, \quad (27)$$

is the requested average value of the mass quadrupole moment and C_q is the quadrupole stiffness constant.

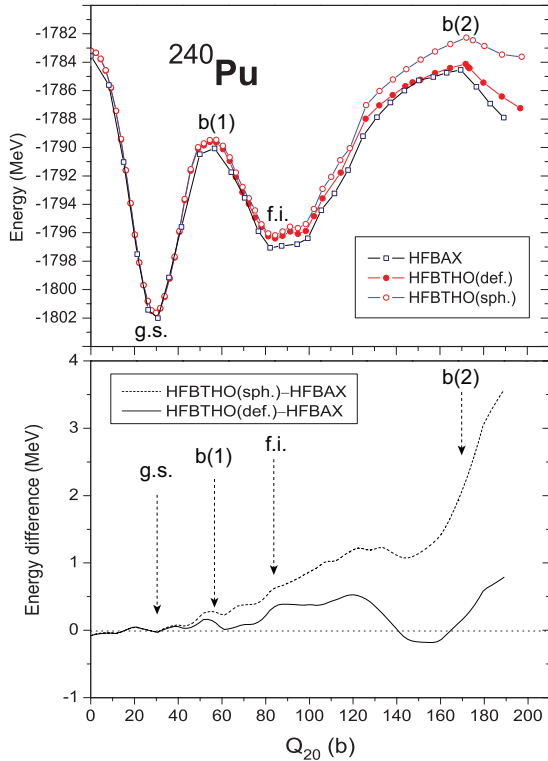


FIG. 7: (Color online) Top: axial, reflection-symmetric fission path of ^{240}Pu (top) calculated with HFB-AX and HFBTHO (in a spherical and stretched HO basis). Bottom: the difference between HFBTHO and HFB-AX results (normalized to zero at the ground-state configuration). The minima and maxima of energy are marked: ground state, g.s.; first barrier, b(1); fission isomer, f.i.; second barrier, b(2).

The constrained HFB-AX calculations for ^{240}Pu were performed in a box of $R=23.4$ fm and $h=0.65$ fm, using a B-spline basis with $M=11$. (For a similar mesh size, the binding energy of ^{120}Sn in HFB-AX agrees with HFBAD within 50 keV.) The HFBTHO calculations were carried out in a typical space of $N_{\text{sh}}=20$ spherical or stretched

HO shells. The mixed pairing interaction is used with the pairing strength adjusted as in Sec. III B for ^{120}Sn . The results are displayed in Fig. 7. The spherical HO basis is unreliable for fission calculations, and the quality of HFBTHO calculations with a stretched basis deteriorates gradually with deformation. That is, the energy error on the first barrier and fission isomer is ~ 100 keV and ~ 400 keV, respectively, and it reaches ~ 500 keV inside the second barrier. These are significant corrections that can impact calculated half-lives for spontaneous fission.

IV. CONCLUSIONS

We developed a 2D coordinate space code HFB-AX using the technique of basis splines. The high accuracy of the code has been demonstrated by benchmarking it against the multi-resolution wavelet method, the HO basis expansion method, and the radial finite difference method. The tests have been carried out for spherical and very deformed configurations of stable and weakly bound nuclei.

A significant numerical speedup of the code makes it a useful tool for nuclear structure calculations of exotic configurations, such as halos and extremely elongated fissioning nuclei. Among the first applications of HFB-AX planned are systematic studies of deformed drip-line systems. The ability of the code to accommodate very large angular momentum cutoffs is crucial in the context of nuclei with large neutron skins and halos, in which the high- j continuum has significant impact on pairing correlations [38].

Other applications involve systematic studies of superdeformed configurations and fission isomers. HFB-AX will also provide systematic energy corrections at large deformations, essential for HFB models of fission based on HO expansion. The differences seen in Fig. 7 are expected to appreciably impact the predicted spontaneous fission half-lives.

In this work, reflection-asymmetric and triaxial deformations, important in realistic fission calculations, have not been investigated. We are currently developing a symmetry-free coordinate-space 3D HFB solver based on the multi-resolution wavelet method. The HFB-AX code reported in this paper will provide crucial benchmark tests for the general-purpose wavelet HFB framework.

Acknowledgments

This work was supported in part by the U.S. Department of Energy under Contract Nos. DE-FG02-96ER40963 (University of Tennessee), DE-AC05-00OR22725 with UT-Battelle, LLC (Oak Ridge National Laboratory), DE-FG05-87ER40361 (Joint Institute for Heavy Ion Research), and DE-FC02-07ER41457 with UNEDF SciDAC Collaboration. Computational resources were provided by the National Center for

-
- [1] *RIA Theory Bluebook: A Road Map*, http://www.ornl.gov/ria/RIATG/Blue_Book_FINAL.pdf.
- [2] G.F. Bertsch, D.J. Dean, and W. Nazarewicz, SciDAC Review, Winter 2007, p. 42.
- [3] W. Kohn and L.J. Sham, Phys. Rev. A **140**, 1133 (1965).
- [4] M. Bender, P.-H. Heenen, and P.-G. Reinhard, Rev. Mod. Phys. **75**, 121 (2003).
- [5] *Extended Density Functionals in Nuclear Structure Physics*, ed. by G.A. Lalazissis, P. Ring, and D. Vretenar (Springer Verlag, 2004).
- [6] E. Perlińska, S. G. Rohoziński, J. Dobaczewski, and W. Nazarewicz, Phys. Rev. **C69**, 014316 (2004).
- [7] J. Dobaczewski, H. Flocard, J. Treiner, Nucl. Phys. A **422**, 103 (1984).
- [8] J. Dobaczewski, W. Nazarewicz, T.R. Werner, J.F. Berger, C.R. Chinn, and J. Dechargé, Phys. Rev. C **53**, 2809 (1996).
- [9] V. Blum, G. Lauritsch, J.A. Maruhn, and P.-G. Reinhard, J. Comput. Phys. **100**, 364 (1992).
- [10] J. Terasaki, P.-H. Heenen, H. Flocard, and P. Bonche, Nucl. Phys. A **600**, 371 (1996).
- [11] P.-H. Heenen, P. Bonche, J. Dobaczewski, H. Flocard, S.J. Krieger, J. Meyer, J. Skalski, N. Tajima, and M.S. Weiss, Proc of Int. Workshop on Nuclear Structure Models, eds. R. Bengtsson, J. Draayer and W. Nazarewicz (World Scientific, Singapore, 1992), p 3.
- [12] P. Bonche, H. Flocard, and P.H. Heenen, Comput. Phys. Comm. **171**, 49 (2005).
- [13] K. Bennaceur, and J. Dobaczewski, Compt. Phys. Comm. **168**, 96 (2005).
- [14] E. Terán, V.E. Oberacker, and A.S. Umar, Phys. Rev. C **67**, 064314 (2003).
- [15] V.E. Oberacker, A.S. Umar, E. Terán, and A. Blazkiewicz, Phys. Rev. C **68**, 064302 (2003).
- [16] A. Blazkiewicz, V.E. Oberacker, A.S. Umar, and M. Stoitsov, Phys. Rev. C **71**, 054321 (2005).
- [17] <http://www.csm.ornl.gov/ccsg/html/projects/madness.html>
- [18] G.I. Fann, R.J. Harrison, G. Beylkin, J. Jia, R. Hartman-Baker, W.A. Shelton, and S. Sugiki, J. Phys. Conf. Ser. **78**, 012018 (2007)
- [19] P. Ring, P. Schuck, *The nuclear many-body problem*, Springer-Verlag, 1980.
- [20] J. Dobaczewski, M.V. Stoitsov, and W. Nazarewicz, AIP Conference Proceedings, **726**, 51 (2004).
- [21] M.V. Stoitsov, J. Dobaczewski, W. Nazarewicz, P. Ring, Comp. Phys. Commun. **167**, 43(2005).
- [22] J. Dobaczewski, W. Nazarewicz, and M.V. Stoitsov, Eur. Phys. J. A **15**, 21 (2002).
- [23] J. Dobaczewski, W. Nazarewicz, and P.-G. Reinhard, Nucl. Phys. A **693**, 361 (2001).
- [24] <http://www.netlib.org/lapack/>
- [25] D.D. Johnson, Phys. Rev. B **38**, 12807 (1988).
- [26] A. Baran, A. Bulgac, M. McNeil Forbes, G. Hagen, W. Nazarewicz, N. Schunck, and M.V. Stoitsov, arXiv:0805.4446, Phys. Rev. C, in press (2008).
- [27] E. Chabanat, P. Bonche, P. Haensel, J. Meyer, and R. Schaeffer, Nucl. Phys. A **635**, 231(1998).
- [28] R.J. Harrison, G.I. Fann, T. Yanai, Z. Gan, and G. Beylkin, J. Chem. Phys. **121**, 11587 (2004)
- [29] J. A. Maruhn and W. Greiner, Z. Physik **251**, 431(1972).
- [30] M. Marini, F. Pistolesi, and G.C. Strinati, Eur. Phys. J. B **1**, 151 (1998).
- [31] T. Papenbrock and G.F. Bertsch, Phys. Rev. C **59**, 2052 (1999).
- [32] P.J. Borycki, J. Dobaczewski, W. Nazarewicz, and M.V. Stoitsov Phys. Rev. C **73**, 044319 (2006).
- [33] J. Meng and P. Ring, Phys. Rev. Lett. **77**, 3963 (1996).
- [34] K. Bennaceur, J. Dobaczewski, and M. Płoszajczak, Phys. Lett. B **496**, 154 (2000).
- [35] J.Terasaki and J.Engel Phys. Rev. C **76**, 044320 (2007).
- [36] J. Margueron, H. Sagawa, and K. Hagino, Phys.Rev. C **77**, 054309 (2008).
- [37] M. Stoitsov, N. Michel, and K. Matsuyanagi, Phys. Rev. C **77**, 054301 (2008).
- [38] V. Rotival, K. Bennaceur, and T. Duguet, arXiv:0711.1275, (2007); V. Rotival and T. Duguet, nucl-th/0702050 (2007), to be published in Phys. Rev. C.